Hybrid experimental-machine learning evaluation of fractal geometrical effects on rammed earth materials strength

Ahmad Morsel, Bassel Habeeb, Claire Silvani, Emilio Bastidas-Arteaga, Laurent Briancon

To cite this version:

Ahmad Morsel, Bassel Habeeb, Claire Silvani, Emilio Bastidas-Arteaga, Laurent Briancon. Hybrid experimental-machine learning evaluation of fractal geometrical effects on rammed earth materials strength. Construction and Building Materials, 2026, 527, pp.146476. ⟨10.1016/j.conbuildmat.2026.146476⟩. ⟨hal-05632271⟩

HAL Id: hal-05632271

https://cnrs.hal.science/hal-05632271v1

Submitted on 25 May 2026

Hybrid experimental-machine learning evaluation of fractal geometrical effects on rammed earth materials strength

Ahmad Morsel[1,2]*, Bassel Habeeb[3], Claire Silvani[1], Emilio Bastidas-Arteaga[3],
Laurent Briancon[1]

[1] INSA Lyon, GEOMAS, Villeurbanne 69621, Lyon, France.
[2] University of Lyon, LabEx IMU, UMR5259, Villeurbanne 69621, Lyon, France.
[3] Laboratory of Engineering Sciences for the Environment, UMR CNRS 7356, La Rochelle University, France.

Abstract

Rammed earth is a sustainable construction material that aligns with circular-economy principles, as soil is taken from excavation and reused to build earthen structures. Evaluating and improving compressive strength is essential to ensure structural stability. An Apollonian Packing (AP) mathematical model is applied to regulate the arrangement and size of particles to match a specified geomatric fractal dimension (D_f).

Compressive specimens were prepared using particle size distributions based on Apollonian Packing and compared with specimens made from naturally graded soils. Experimental results showed that specimens with $D_f = 2.75$ exhibited compressive strength approximately 18% higher than those with $D_f = 2.5$. In addition, AP specimens demonstrated improved repeatability and reduced mechanical variability. Specimens produced from three different natural soils showed similar compressive strength values for the same D_f, indicating that mechanical behavior is governed primarily by particle size distribution rather than mineralogical composition under dry condition.

The results were further analyzed using a machine-learning approach based on an artificial neural network multi-layer perceptron model. The model successfully captured interactions between microstructural descriptors and accurately predicted compressive strength for soil specimens, achieving a mean absolute error of 0.014 MPa.

This study combines fractal-based Apollonian Packing with machine learning to enhance the strength and reliability of rammed earth structures, resulting in a transferable and soil-independent predictive framework.

Keywords: Apollonian Packing ; Rammed earth ; Compressive strength ; Geometric fractal dimension ; Multilayer perceptron model ; Natural soils.

1 Introduction

Rammed-earth construction is one of the oldest and widely used construction techniques that has been used for thousands of years [12]. The method essentially consists of compacting the earth

---

[*] Corresponding author. E-mail address: ahmad.morsel@insa-lyon.fr ¸

into a formwork in which walls carry loads. In addition to being environmentally friendly, raw earth material is highly sustainable because it can be found locally on all five continents [22, 36]. Made from naturally available materials, rammed earth has been used in iconic buildings such as the Great Mosque of Djenné in Mali [15], the Great Wall of China [18], and the Alhambra in Spain [17], and in modern construction [20]. These examples demonstrate the strength and adaptability of rammed earth, both as a building material in modest homes and monumental structures.

Using raw earth as an alternative building material can significantly reduce the consumption of cement and steel. These materials' production accounts for 7–9% of direct global greenhouse gas emissions [42] and about 7% of global CO_2 emissions [21]. In addition, raw earth provides advantages in natural thermal insulation and breathability, while supporting local economies through the use of locally available resources and traditional building techniques. In this context, integrating raw earth into current construction methods represents a relevant strategy to reduce environmental impacts while supporting economic sustainability and preserving cultural heritage [33].

Although numerous studies have examined the mechanical behavior of rammed earth, yet there is still no standardized testing protocol for material characterization like for concrete or other engineer geomaterials (e.g., national building codes, uniform mix-design standards). Among the mechanical properties of rammed earth, compressive strength is primarily used to characterize it, since this material must withstand uniaxial compressive stresses during operation. However, compressive strength values are highly sensitive to several interacting parameters, such as density, clay type, particle size and arrangement, and water content used in specimen fabrication.

Anglade [3] studied the compressive strength of specimens composed of fine particles (kaolonite clay) and sands and shows that the compressive strength increased approximately linearly with sand content—and therefore with dry density—for both dry and moist specimens. While many studies confirm that dry density influences strength, it is not the only governing factor. Prior research [8, 26, 31] has shown that, for soils with identical constituents but varying proportions, compressive strength rises with dry density; however, other studies [3, 9, 27, 35] show that that density alone cannot be used to predict strength. Other works highlight the influence of clay content and clay mineralogy [11, 34], soils containing swelling clays exhibit higher strengths than those with non-swelling clays. Water content also significantly affects strength, with higher moisture levels reducing compressive resistance, a trend widely reported in the literature [1, 39]. This is commonly attributed to capillary pressures, which increase during drying and enhance cohesion. In summary, compressive strength depends on dry density, clay content and type, particle size and water content.

In earth materials, the internal structure (e.g., the arrangement and size distribution of particles) strongly influences the mechanical behavior of rammed earth materials. However, soil behavior is also affected by the mineralogical nature of the clay fraction, which can introduce physico-chemical interactions such as electrostatic attraction, water adsorption, and interparticle bonding. These mechanisms may significantly affect shear strength and plasticity in clay-rich soils. In the present study, the focus is placed specifically on the geometrical aspect of particle organization, namely the particle size distribution and packing structure. Consequently, the proposed framework does not explicitly account for mineralogical clay interactions but rather investigates how controlled particle gradation and packing geometry influence the mechanical response.

To study this geometrical effect, particle size distribution is controlled using the Apollonian Packing (AP) concept. AP model, named after the ancient Greek mathematician Apollonius of Perga, describes a fractal, space-filling arrangement in which progressively smaller particles occupy the voids between larger ones [16]. Such arrangements generate a self-similar structure characterized by a geometric fractal dimension that quantifies the hierarchical distribution of particle sizes within the packing. This approach provides a mathematical framework to investigate how particle packing geometry may influence the mechanical properties of rammed earth materials [4, 30].

Despite growing interest in the application of fractal geometry to granular materials, the particular impact of the Apollonian packing has on rammed earth concerning its compression strength has not been studied. Although several studies have focused on the fractal nature of particle crushing and its implications for sand and soil compression [6, 7, 13, 32], few have considered the implications of Apollonian packing for mechanical properties [4, 24]. This gap in the literature calls for systematic investigation in regard to the arrangement of particles, the void space it creates, and the final overall mechanical behavior of rammed earth materials.

In recent years, machine learning has been intensively applied in materials characterization due to their ability to learn complex relationships from data, linking the characteristics of materials and micro-structural features to mechanical properties [25]. In addition, machine learning methods have successfully identified defects that are difficult to detect through manual analysis and have shown remarkable improvements in predicting extreme events [23]. Neural Network method, in particular, is becoming a powerful tool in materials characterization by enabling the extraction of complex-nonlinear relationships within the composition, structure, physical, and mechanical characteristics of the materials [41]. The application of this method reveals the hidden patterns rising from the complex interactions between the characteristics and variability of the materials, improving the interpretation of the results [38]. The application of this method has efficiently improved the evaluation of materials and the prediction of the behaviour of a material under certain conditions.

This paper investigates the characteristics of rammed earth specimens following the Apollonian packing concept. This aims at understanding the influence of particles arrangement and size distribution, thus the fractal dimension on the mechanical performance of the materials experimentally. Moreover, a numerical approach following a Neural Network method is considered to reveal the underlying patterns of complex relationships within the characteristics of the rammed earth materials and the resulting compressive strength. The findings will improve our understanding of how internal structures affect the building of rammed earth.

The paper is structured as follows. Section 2 presents the derivation of the Apollonian packing model based on a power-law formulation, the soil preparation procedure, and the machine-learning-based approach for predicting compressive strength. Then Section 3 describes the characterization of the natural soils, followed by specimens preparation and experimental setup (Section 4). Then, Section 5 presents and discusses the experimental and numerical results, including a comparison between specimens made with natural soils with to specimens based on Apollonian model. Finally, the paper concludes with an analysis of the influence of fractal dimension on compressive strength and result repeatability.

2 Methodology

In this Section, we present the concept of Apollonian packing (Section 2.1), which is employed as a theoretical framework for designing specimens with specific particle size distributions. This is followed by introducing the machine learning method, i.e., Multi-Layer Perceptron (Section 2.2), which is adopted to identify the underlying complex relationship within the materials characteristics and their mechanical behavior.

2.1 Apollonian methods

The objective of this section is to develop a practical method for reconstructing a soil mixture based on a given natural soil. The reconstructed soil follows a defined particle-size distribution characterized by a geometric fractal dimension D_f according to the Apollonian Packing (AP) concept.

In fractal particle systems, the fractal dimension D_f describes how particle sizes are distributed across different scales. Physically, D_f reflects the relative proportion of coarse and fine particles within the mixture. Lower D_f values generally correspond to coarser gradations dominated by larger particles, whereas higher D_f values indicate a greater proportion of fine particles that can fill the voids between larger grains. As a result, increasing D_f tends to promote more efficient packing of particles, although the resulting density also depends on fines content, compaction conditions, and soil fabric.

Based on this principle, the AP framework is used to derive the required mass m_i of each particle-size fraction, enabling the preparation of a soil mixture with a specified total mass and target D_f. The AP concept follows a power-law linking particle size to particle number or mass, and consequently to the occupied volume. Subsequently, these relationships are used to compute the mass m_i associated with each sieve fraction of the reconstructed soil. The power-law can then be expressed as

$$N(d > d_0) \propto d_0^{-D_f}, \tag{1}$$

where d_0 is a reference soil particle diameter, $N(d > d_0)$ is the cumulative number of particles with diameter greater than d_0, and D_f is the geometric fractal dimension, which characterizes the particle size distribution.

In a three-dimensional system, D_f usually ranges between 2.0 and 3.0. A low value of D_f (e.g., 2.2) reflects a poorly graded material with less fine material and more larger particles, while a large value (e.g., 2.9) reflects more well-graded material with more fines that effectively fill the voids between larger particles [19, 44, 45].

In AP, the cumulative volume $V(d > d_0)$ of all particles with diameter greater than d_0 scales as

$$V(d > d_0) \propto d_0^{3-D_f}, \tag{2}$$

where 3 is the dimension of the Euclidean space. For instance, if $D_f = 2.5$, this becomes

$$V(d > d_0) \propto d_0^{0.5}. \tag{3}$$

This indicates that larger particles dominate the total occupied volume, while fine particles primarily fill the voids and contribute comparatively less to the overall mass and volume (see Figure 1).

2.1.1 Preparation of soil mixture based on the Apollonian concept

In this study, we consider three natural soils, where our objective is to create a soil mixture (for each soil type) whose particle-size distribution follows a power-law relationship characterized by a specified fractal dimension. In our case, we used a fractal dimension of 2.5, which represents an average for soils in a three-dimensional system.

We used Eq. 1 and Eq. 3 to derive the mass m_i assigned to each particle-size d_i. Assuming spherical particles with constant density ρ_s, the mass of a particle is proportional to its volume,

$$m_i \propto V(d_i)\,\rho_s. \tag{4}$$

Using the Apollonian scaling of cumulative volume, $V(d > d_0) \propto d_0^{3-D_f}$, and adopting $D_f = 2.5$, the volume associated with particles of representative size d_i scales as:

$$V(d_i) \propto d_i^{0.5}. \tag{5}$$

Consequently, the mass contribution of particles of size d_i also scales as

$$m_i \propto d_i^{0.5}. \tag{6}$$

In practice, particles are grouped into discrete size classes corresponding to sieve fractions. For each sieve fraction, a characteristic diameter d_i (taken as the geometric mean of the sieve bounds) is used to approximate the continuous Apollonian distribution. The total mass of the soil sample is therefore expressed as:

$$m_{\text{total}} = \sum_{i=1}^{n} m_i \propto \sum_{i=1}^{n} d_i^{0.5}, \tag{7}$$

where n is the number of sieves. To obtain a normalized mass distribution while preserving the Apollonian scaling implied by Eq. 7, the mass assigned to each particle-size is given by

$$m_i = m_{\text{total}} \cdot \frac{d_i^{0.5}}{\sum_{i=1}^{n} d_i^{0.5}}, \tag{8}$$

where m_i is the mass of particles of size d_i and $m_{\text{total}} = 5500$ g (approximation of mass we need to prepare one specimen). Soil mixture was prepared by sieving our natural soil following a standard sieve test to segregate particles into various size fractions (e.g. 10 mm, 5 mm, 2.5 mm, 1.25 mm, etc.). We assume that a representative particle size for each fraction is the average of the two consecutive sieve sizes. For instance, for the soils retained between 20 mm and 10 mm, we choose 15 mm as our particle size.

This formulation conserves the total specimen mass while ensuring that the reconstructed soil mixture follows the prescribed Apollonian fractal dimension. Figure 1 presents the cumulative mass passing calculated based on Eq. 8 and the proposed sieve size (or diameter of soil particles). Higher D_f means that the material has more fine particles and consequently better void filling.

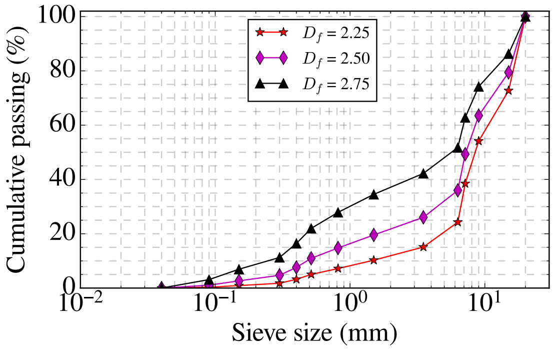

Figure 1: Particles size distribution of soil based on Apollonian model with different geometric fractal dimension (theoretical).

2.2 Machine Learning

2.2.1 Background

This study employs a multilayer perceptron model (MLP) [37] to provide a robust modeling framework for material characterization (Section 3) and the prediction of the mechanical properties (Section 5.1.2). This model is a feed-forward artificial neural network model composed of successive layers, i.e., input, hidden, and output layers, where layers are parameterized by weight matrices and bias vectors. The applied model incorporates an optimal architecture (Figure 2) consisting of three hidden layers l comprising 50, 25 and 5 neurons, respectively. The optimal neural network architecture was determined using a grid-search-based hyperparameter optimization. The search space included multiple network depths and neuron configurations, as well as different activation functions and optimization algorithms. Model performance was evaluated using the mean squared error as the optimization criterion.

During training, the MLP learns the relationship between the material input features and the target, i.e., mechanical property, through iterative forward and backward propagation phases. Within the forward propagation, each neuron computes a weighted sum of the inputs from the previous layer considering the additional bias term and applies a nonlinear activation function to produce its output. This process continues through all hidden layers until the output layer, where the network generates a prediction of the target. This predicted value is then compared to the experimental measured target through the loss function, i.e., mean squared error augmented by an L2 regularization term to quantify the prediction error. This is followed by the backpropagation phase, where the loss gradients of the network parameters are calculated by applying the chain rule, indicating the direction of each weight and bias to be adjusted to minimize the prediction error. These gradients pass through an optimization algorithm, i.e., Limited-memory Broyden–Fletcher–Goldfarb–Shanno (L-BFGS) [28], to update the model parameters until convergence is achieved. This cycle of forward propagation, loss evaluation, backward propagation, and weight updating continues iteratively until the model reaches optimal performance.

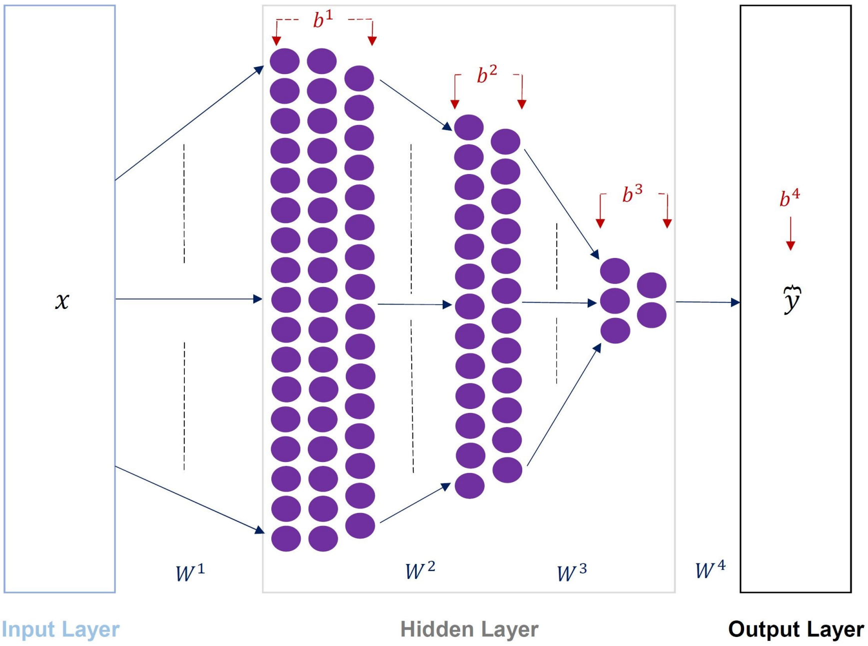

Figure 2: Architecture of the Neural Network.

2.2.2 Detailed description

Let the input vector be represented by $x \in \mathbb{R}^d$. For each hidden layer l, define the weight matrix W^l and the bias vector b^l. The network architecture of three hidden layers l consists of 50, 25, and 5 neurons, respectively. The pre-activation input a^l produced by the i^{th} neuron of that layer l, i.e., $a^{[1]} \in \mathbb{R}^{50}$, $a^{[2]} \in \mathbb{R}^{25}$, and $a^{[3]} \in \mathbb{R}^5$, respectively, is calculated as the weighted sum W of the previous layer's output (x for $l = 1$, h^l for $l > 1$) and its bias term. The non-linear activation function σ is then applied element-wise on each neuron's pre-activation value $a_i^{[l]}$ to obtain the post-activation output vector h^l for each layer l.

$$a^{[l]} = W^{[l]} h^{[l-1]} + b^{[l]}, \qquad h^{[0]} = x. \tag{9}$$

$$h_i^{[l]} = \sigma\left(a_i^{[l]}\right) = \sigma\left(W^{[l]} h^{[l-1]} + b^{[l]}\right) = \max(0,\, a_i^{[l]}). \tag{10}$$

The output of the final layer $\hat{y}$ is a regression prediction through a linear activation function ρ for the final hidden layer to predict continuous values.

$$\hat{y} = \rho\left(a^{[4]}\right) = W^{[4]} h^{[3]} + b^{[4]}. \tag{11}$$

$$\hat{y} = W^{[4]}\, \sigma\Big(W^{[3]}\, \sigma\big(W^{[2]}\, \sigma\big(W^{[1]} x + b^{[1]}\big) + b^{[2]}\big) + b^{[3]}\Big) + b^{[4]}. \tag{12}$$

Before training, the input features are standardized to zero mean and unit variance to prevent features with large magnitudes dominating the loss and to improve the conditioning of the optimization. The parameters of the model θ (Eq.(14)) consist of weights $W^{[l]}$ and bias $b^{[l]}$ in each layer l, which are learned by minimizing the mean squared error between the predicted values $\hat{y}_i$ and the true values y_i. Incorporating the L2 regularization penalty coefficient on each weight mitigates overfitting.

$$\theta = \{W^{[l]}, b^{[l]}\}_{l=1}^{4} \tag{13}$$

The gradients of the loss function L (Eq. (14)) are calculated through the backpropagation phase with respect to the network parameters (θ). The error for the output pre-activation layer $\delta^{[a]}$ (Eq. (15)) is the derivative of the loss function with respect to the output of the pre-activation input layer $a_i^{[l]}$. This error is propagated backward through the hidden layers using the chain rule. At each layer, the derivative of the nonlinear activation function $\sigma'(a_i^{[l]})$ (Eq. (16)) determines the error distribution through each neuron. Once the layer-wise errors $\delta^{[l]}$ ((Eq. (17)) are obtained, the gradients with respect to the weight matrices $\frac{\partial L}{\partial W^{[l]}}$ and bias vectors $\frac{\partial L}{\partial b^{[l]}}$ are calculated (Eqs. (18 and 19)).

$$L(\theta) = \frac{1}{N}\sum_{i=1}^{N}(y_i - \hat{y}_i)^2 + \alpha \sum_{l=1}^{4}\|W^{[l]}\|_2^2\,, \tag{14}$$

$$\delta^{[a]} = \frac{1}{N}(\hat{y}_i - y_i) \tag{15}$$

$$\sigma'\left(a_i^{[l]}\right) = \begin{cases} 1, & a_i^{[l]} > 0, \\ 0, & a_i^{[l]} \leq 0 \end{cases} \tag{16}$$

$$\delta^{[l]} = \left(W^{[l+1]}\right)^T \delta^{[l+1]} \odot \sigma'\left(a^{[l]}\right), \qquad l = 3, 2, 1 \tag{17}$$

$$\frac{\partial L}{\partial W^{[l]}} = \delta^{[l]}\left(h^{[l-1]}\right)^T + 2\alpha W^{[l]} \tag{18}$$

$$\frac{\partial L}{\partial b^{[l]}} = \delta^{[l]} \tag{19}$$

where N is the number of training specimens, and α is the regularization coefficient.

The gradients of the loss function $\frac{\partial L}{\partial W^{[l]}}$ and $\frac{\partial L}{\partial b^{[l]}}$ are updated through the L-BFGS optimizer [28], which is a quasi-Newton optimization method that updates the parameter vector by iteratively approximating the inverse Hessian of the loss function. The parameter θ updated at iteration k (Eq. (20)) is obtained by multiplying the gradient $\nabla L(\theta_k)$ (Eq. (21)) by an approximate inverse Hessian matrix H_k, which is updated recursively using the parameter displacement Hs_j and gradient displacement Hy_j. This approach enables L-BFGS to achieve efficient and stable convergence.

$$\theta_{k+1} = \theta_k - H_k \nabla L(\theta_k) \tag{20}$$

$$g_k = \nabla L(\theta_k) = \begin{bmatrix} \operatorname{vec}\left(\frac{\partial L}{\partial W^{[l]}}\right) \\ \frac{\partial L}{\partial b^{[l]}} \end{bmatrix} \Bigg|_{l=1}^{4} \tag{21}$$

$$Hs_j = \theta_{j+1} - \theta_j, \qquad Hy_j = g_{j+1} - g_j \tag{22}$$

3 Materials characterization

This section presents the soils used in the compression tests, namely three natural soils denoted CLM, STA, and SPC. These soils were collected from three locations in southeastern France within the Auvergne–Rhône–Alpes region: Saint-Antoine-l'Abbaye (STA), Saint-Pierre-de-Chandieu (SPC), and Cruzilles-lès-Mépillat (CLM). These sites were selected to provide soils representative of typical earth materials used in regional rammed earth construction (see Figure 3). Several material characterization tests including sieve analysis, modified Proctor, pycnometer measurements, and Blue methylene tests were conducted to determine the physical and mechanical properties of the natural soils.

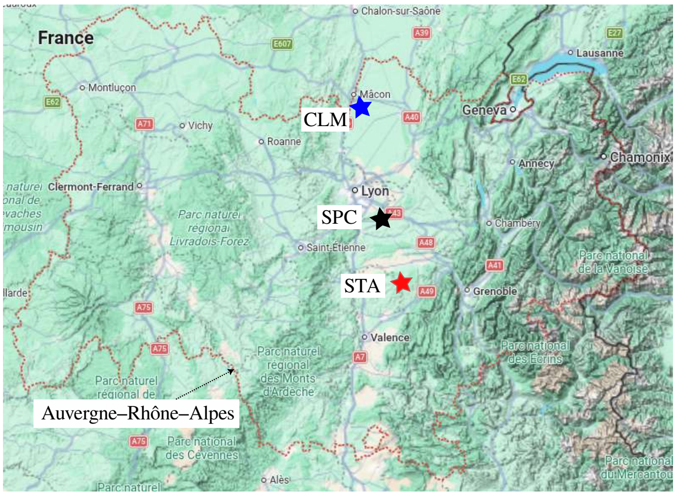

Figure 3: The location of the three natural soils CLM, STA, and SPC.

3.1 Sieve analysis

All soils were first presieved to remove particles above 2 cm (see Figure 4a). Then, wet sieving was performed using water to help disaggregate fine material and keep it from clumping. The procedure begins with preparing and weighing a sample and then soaking the sample in water to break aggregate forms. The resultant slurry is poured through a stack of sieves that are arranged from coarse to fine, while continuously rinsing until the wash water runs clear indicating all the fine material has washed through. The material retained on each sieve is carefully dried in the oven at 105°C for 24 hours, weighed, and recorded. Finally, the percent retained and percent passing is calculated for each sieve to determine a particle size distribution curve as shown in Figure 4b.

The soil below 0.2 mm was tested with laser diffraction (Mastersizer machine [29]). The

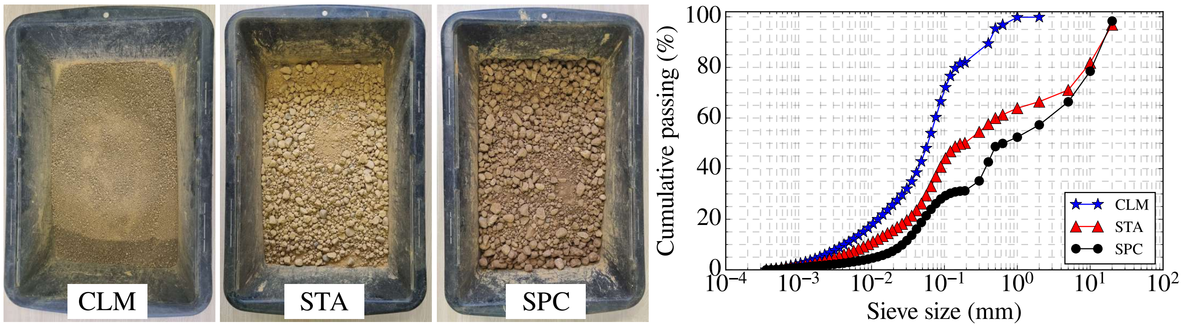

(a) (b)

Figure 4: Three natural soils CLM, STA, and SPC (a), and particle size distribution curves (b).

Mastersizer provides particle size distributions expressed as volume percentages. To ensure consistency with the sieve analysis results, which are expressed as cumulative mass passing, the laser diffraction data were converted to mass-based values. This conversion was performed assuming a constant particle density across the analyzed size fractions, which allows the volume fraction to be considered equivalent to the mass fraction. The resulting distribution was then integrated with the sieve analysis results to produce the cumulative mass passing curve shown in Figure 4b.

From this figure the results indicate notable variations in the particle size distribution among the three different soils (CLM, SPC, and STA). For CLM soil, it is apparent that the soil is primarily fine-grained, as most of the material that lies within the range of fine sand to silt. The sieve analysis of the SPC soil shows that it retained the coarser particles, and these particles are the most prominent in the distribution of the soil, classifying it as a coarse-grained. The STA sieve analysis shows an intermediate gradation of coarse and fine fractions in approximately equal proportions. This is indicative of a naturally occurring, well-graded, a sandy gravel soil type. Overall, the CLM soil is the finest, the SPC soil is the coarsest, and the STA soil is intermediate (the most consistently graded).

Using Particle Size Distribution (PSD) data the coefficient of uniformity and curvature were calculated for the three soils. These parameters provide quantitative information regarding the uniformity of particle sizes, as shown in Table 1.

Table 1: Grain size distribution parameters for CLM, STA, and SPC soils.

Soil Sample	D_{10} (mm)	D_{30} (mm)	D_{50} (mm)	D_{60} (mm)	C_u	C_c
CLM	0.0042	0.026	0.0585	0.0763	18.2	2.2
STA	0.009	0.058	0.18	0.5	55.5	0.75
SPC	0.028	0.125	0.65	2.6	92.8	0.2

where D_{10}, D_{30}, D_{50}, and D_{60} are the particle diameters corresponding to 10%, 30%, 50% and 60% passing respectively. C_u is the coefficient of uniformity, and C_c is the coefficient of curvature.

The results in Table 1 confirm the distinct gradation characteristics observed in the sieve analysis. The CLM sample exhibits $C_u = 18.2$ and $C_c = 2.2$, satisfying the criteria for a well-graded fine soil ($C_u > 6$ and $1 \leq C_c \leq 3$ [5]). In contrast, SPC shows a very high C_u value (92.8) but a low C_c (0.2), indicating a gap-graded coarse material dominated by gravel and sand fractions. The STA sample presents intermediate values ($C_u = 55.5$, $C_c = 0.75$), suggesting a moderately graded sandy gravel with a smoother particle size distribution than SPC. These quantitative parameters align with the sieve analysis trends, where CLM was identified as fine-grained, SPC as coarse-grained, and STA as an intermediate, well-balanced material.

3.2 Bulk and particle density

The Modified Proctor [2], test was conducted to determine the maximum dry density and the optimum moisture content required to prepare the specimens (see Figure 5). This test was chosen compared to the standard one, because rammed earth requires high compacted energy to obtain high densities. This test provides a better reflection of field conditions for this application.

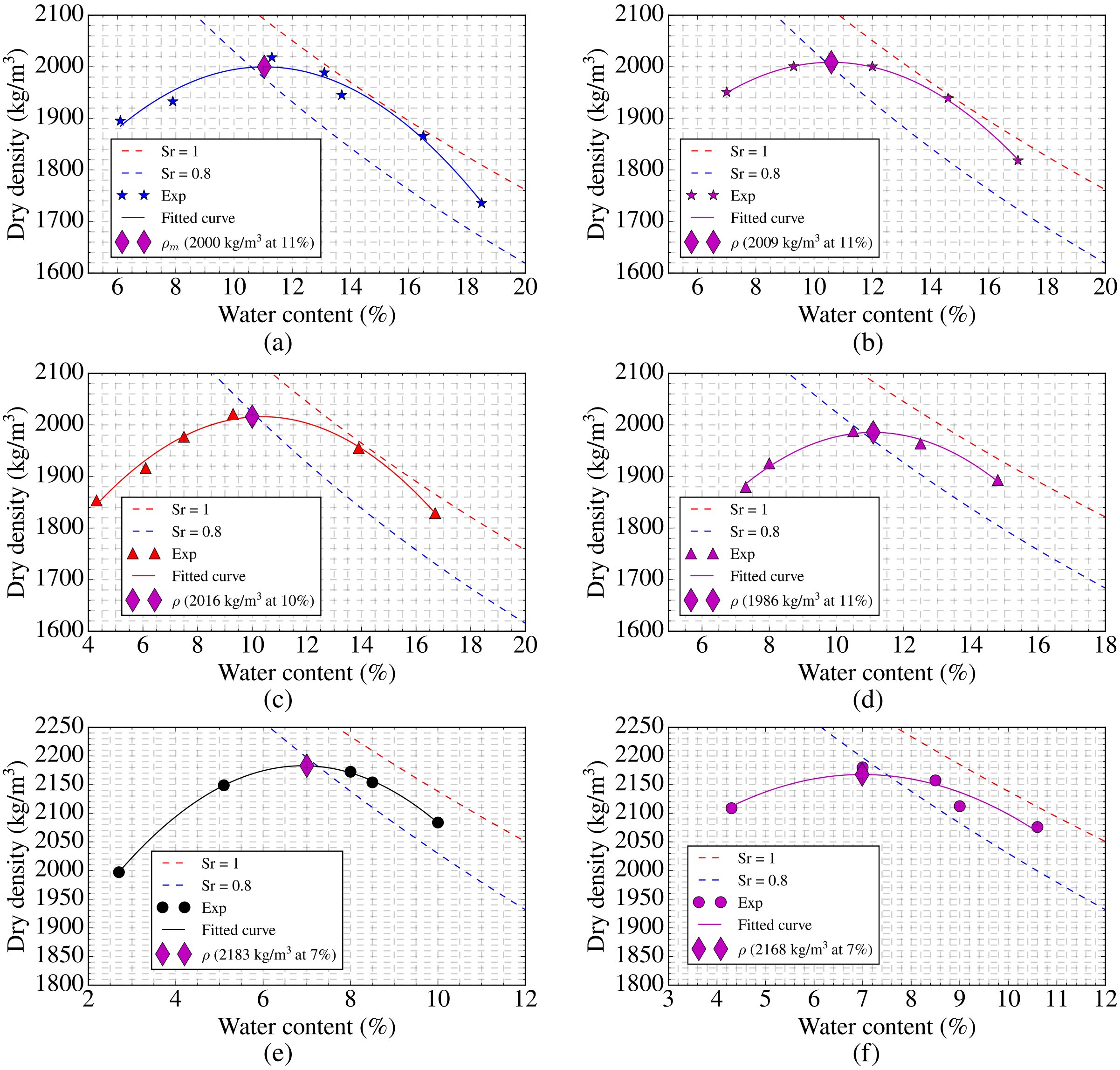

Figure 5: Modified proctor: (a) CLM soil, (b) CLM-AP soil, (c) STA soil, (d) STA-AP soil, (e) SPC soil, and (f) SPC-AP soil.

The densities values obtained from the modified proctor and pycnometer tests are summarized in Table 2. The bulk densities with and without the application of the AP concept are close, where it is slight lower for AP in case of STA and SPC natural soils. We determine the particle density of soil ρ_s using the pycnometer test, which allows to calculate the porosity n of the specimens prepared with the optimum values from the modified proctor test, enabling the assessment of packing density. For repeatability, we used five Pycnometer's units (50 ml). Soil was sieved (less to 2 mm) and dried in the oven at 105°C for 24 hours. The porosity is computed as $n = 1 - \frac{\rho_b}{\rho_s}$, and the results are given in Table 2.

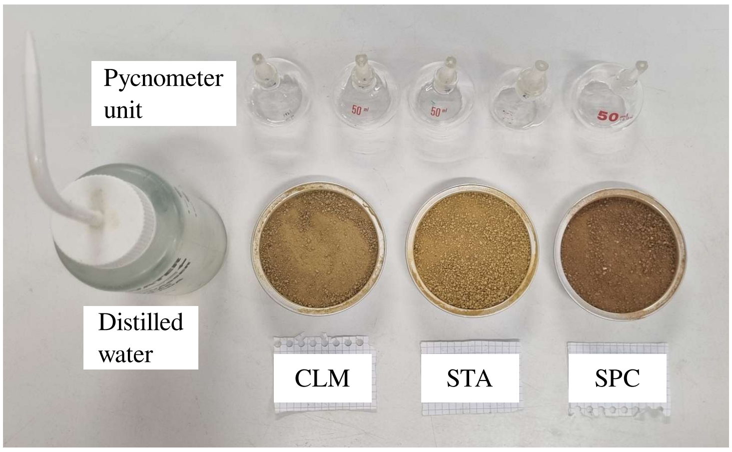

Figure 6: Pycnometer test soils and setup.

Table 2: Summary of bulk densities ρ_b and water contents w for CLM, STA, and SPC soils, with and without AP.

Soil type	ρ_b (kg/m^3)		w (%)		ρ_s (kg/m^3)	n (%)
	without AP	with AP	without AP	with AP		
CLM	2000	2009	11	11	2717	26.4
STA	2016	1986	10	11	2713	25.8
SPC	2183	2168	7	7	2722	19.8

The results of modified proctor and pycnometer indicate a significant difference in the physical properties of the three soils. SPC has the greatest bulk density and the lowest optimum water content, which is consistent with its low porosity (19.8%) and has greater particle density, reflecting an efficient compaction of coarse-grained soil. STA would be characterized as intermediate compared with the other two soils (lower bulk density, optimum water content, and porosity) given the grain-size range of the material is balanced. CLM has the lowest bulk density and the highest optimum water content. As indicated by the porosity values (26.4%), the finer texture of this soil requires more water to properly compact. Thus, soils with lower porosity have courser grains (SPC), allowing the material to compact more tightly and with lower water content. Conversely, CLM has a finer texture and greater porosity, both variables that produced lower density with increased water content.

3.3 Fine characterization

3.3.1 Clay activity

The methylene blue test was performed according to EN 17542-3 on dried soil samples sieved at 5 mm. This test measures the adsorption capacity of the soil by quantifying the amount of methylene blue required to reach surface saturation. The result is expressed as the Methylene

Blue Value (MBV), which corresponds to the mass of methylene blue adsorbed per 100 g of dry soil.

Table 3: Methylene blue test results and derived soil indicators.

Soil type	V_{MB} (mL)	MBV (g/100g)	SSA (m^2/g)	Interpretation
CLM	60	3.00	62.8	Higher clay activity soil
STA	30	1.50	31.4	Low clay activity soil
SPC	27	1.35	28.3	Very low clay activity soil

Note: V_{MB} is the volume of methylene blue solution consumed during the titration, and SSA is the estimated specific surface area derived from MBV.

It should be noted that MBV is determined on the entire soil fraction and therefore reflects the overall adsorption capacity of the soil rather than the mineralogical type of clay present. The specific surface area (SSA) reported in Table 3 was estimated from MBV using SSA $= k \times$ MBV, where k is an empirical proportionality factor relating methylene blue adsorption to the surface area of clay particles.

The results indicate that soil CLM exhibits a higher adsorption capacity and therefore a higher fine particle activity compared with STA and SPC soils. In contrast, STA and SPC show relatively low MBV values, indicating soils dominated by silty particles with limited clay activity.

3.3.2 Plastic and liquid limits

The liquid limit (LL) and plastic limit (PL) indicate the moisture content ranges over which fine-grained soils transition between liquid, plastic, and semi-solid or solid states. The LL was determined using the Casagrande cup method in which a relationship between water content and logarithm of blow counts bunch was established, and the PL was defined by rolling soil threads until the thread crumbled down to a 3 mm diameter. Additionally, the Plasticity Index (PI $=$ LL - PL) provides quantitative measurement of plastic range, and also provide an index of plasticity and clay activity, all the results are summarized in Table 4.

Table 4: Atterberg limits and derived indices.

Soil type	LL (%)	PL (%)	PI (%)
CLM	31.7	23.2	8.5
STA	35.9	29.6	6.3
SPC	25.9	19.9	6.0

The Atterberg limits are consistent with findings of blue methylene tests and surface area values. CLM exhibit moderate plasticity with PI values of 8.5% confirming moderate amount of active fines. SPC and STA has the lowest plasticity values of and 6.3% and and 6.0%, respectively, which reflects limited clay fraction corresponding to a low plasticity silt. The findings confirms that CLM and SPC have the most and less active fine-grained behavior, respectively.

3.4 Soil characterization and link to compressive strength

The combined analysis of all the previous tests provided a consistent classification among the three natural soils CLM, STA, and SPC. The measured physical and physico-chemical properties are interpreted here in terms of their expected influence on the compressive strength of rammed earth.

CLM is the finest of the soils and has a low average particle size D_{50} (0.0585 mm), moderate plasticity ($PI \approx 8.5\%$), and the highest methylene blue value (MBV = 3; SSA $\approx 63\,\mathrm{m}^2/\mathrm{g}$). Consistently, CLM exhibits a relatively high porosity ($n \approx 26.4\%$), reflecting the influence of its fine fraction and high specific surface area under comparable compaction conditions. Its fines show high clay activity. From a mechanical perspective, the high fines content and specific surface area promote interparticle bonding and cohesion, which can contribute to compressive strength under dry or moderately moist conditions. However, the elevated porosity and clay activity also make the compressive strength highly sensitive to water content, leading to a rapid reduction in strength upon wetting.

STA is coarser than CLM with a average size (D_{50} equal to 0.18 mm), low plasticity ($PI \approx 6.3\%$), and lower MBV (1.5; SSA $\approx 31\,\mathrm{m}^2/\mathrm{g}$). Its porosity ($n \approx 25.8\%$) is comparable to that of CLM, but its coarser particle size distribution and lower clay activity favor more efficient particle rearrangement and reduced moisture sensitivity. As a result, its compressive strength, when well compacted, is governed primarily by particle interlocking rather than cohesion.

SPC represents the coarsest material (D_{50} equal to 0.65 mm) and has the lowest MBV (1.35; SSA $\approx 28\,\mathrm{m}^2/\mathrm{g}$), very low plasticity ($PI \approx 6\%$), and the lowest porosity ($n \approx 19.8\%$). It may be classified as a gravelly sand with trace low-activity silt and high drainage capacity. In this case, compressive strength is mainly controlled by particle interlocking and packing density, with limited contribution from fines-induced cohesion.

Overall, these soils illustrate the competing roles of fines-driven cohesion, capillary effects, and coarse-particle packing in controlling the compressive strength of rammed earth, thereby motivating the particle-size distribution optimization approach adopted in this study.

4 Compression tests

This section describes the preparation of compression specimens, the boundary conditions, and the test set-up. Two broad categories of specimens were prepared: (1) based on the natural soils (particle size distribution shown in Figure 4), and (2) AP-based specimens (particle size distribution shown in Figure 1).

All cylindrical specimens (15 cm diameter and 15 cm height) were prepared following a standardized procedure. First, the dry soil was mixed with the required amount of water to reach the optimum moisture content determined from the Proctor test. The moistened soil was sealed in plastic bags and stored for 24 h to allow uniform moisture distribution throughout the material (see Figure 7a). After conditioning, the specimens were compacted in a cylindrical mold in four identical layers, each layer being compacted to achieve the target density (see Figure 7b). Once demolded, the specimens were weighed and their dimensions were measured to determine their bulk density (see Figure 7c). The specimens were air-dried under laboratory conditions for 7 days (approximately 21 °C), allowing gradual moisture reduction after compaction. Subsequently, the specimens were oven-dried at 60 °C for an additional 7 days in order to remove residual moisture and ensure a comparable near-dry condition prior to mechanical testing. This procedure was adopted to minimize the influence of moisture variability and to allow consistent comparison between the different soil mixtures. More details of the specimens are provided in Table 5.

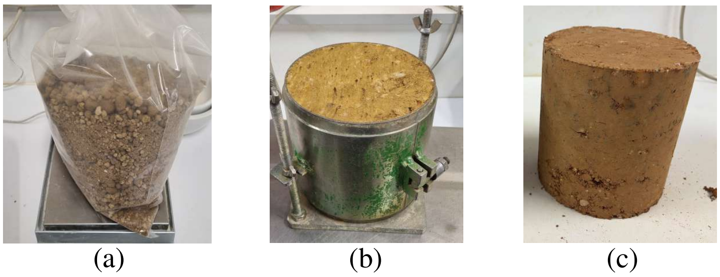
(a) (b) (c)

Figure 7: Specimen preparation procedure: (a) prepare soil, (b) compact specimen, and (c) weight and measure specimen.

A total of fifteen specimens were prepared using the natural soils CLM, STA, and SPC (five for each soil to ensure repeatability). In addition, seventeen specimens were prepared based on the AP models: five CLM-AP ($D_f = 2.5$), three SPC-AP ($D_f = 2.5$), and nine STA-AP (three with $D_f = 2.25$, three with $D_f = 2.5$, and three with $D_f = 2.75$). Examples of AP specimens are shown in Figure 8. All specimens were prepared using the bulk densities and water contents provided in Table 2.

The AP particle size distributions were obtained through dry sieving of the soils after manual disaggregation to break potential aggregates. This procedure was adopted to minimize modifications of the natural soil fabric that could arise from wet dispersion techniques. Although minor aggregation effects cannot be completely excluded, the preparation protocol ensured that the resulting mixtures follow the intended AP gradations.

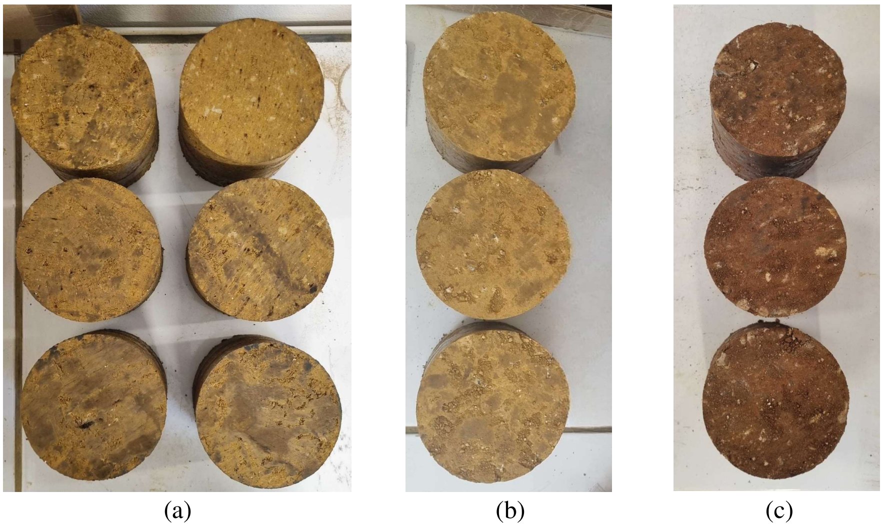
(a) (b) (c)

Figure 8: Prepared specimens followed AP: (a) CLM, (b) STA, and (c) SPC.

The following protocol was applied to ensure a correct installation of the sample in the compression uniaxial machine (see Figure 9): (i) we install an anti-friction system to the upper

Table 5: Average properties of CLM, STA and SPC compression specimens (mean ± SD).

Soil type	θ_f (cm)	h_f (cm)	ρ_b (g/cm^3)	w (%)
CLM	15.16 ± 0.05	15.12 ± 0.03	2.00 ± 0.02	11.05 ± 0.10
CLM-AP	15.16 ± 0.05	15.11 ± 0.04	2.01 ± 0.01	11.02 ± 0.06
STA	15.13 ± 0.06	15.10 ± 0.05	2.01 ± 0.00	10.99 ± 0.05
STA-AP	15.17 ± 0.06	15.13 ± 0.03	1.98 ± 0.00	10.05 ± 0.05
SPC	15.20 ± 0.00	15.22 ± 0.03	2.18 ± 0.00	7.03 ± 0.06
SPC-AP	15.10 ± 0.00	15.10 ± 0.00	2.17 ± 0.00	7.10 ± 0.10

Notes: w is the water content, θ_f and h_f refer to the final diameter and height of each sample, respectively, and ρ_d is the dry density.

and lower parts of the sample which consists of 2–3 mm thick elastomer layer. This layer is inserted in-contact with the specimen up and down, to mitigate the effects of surface roughness on the specimen. (*ii*) A 2 mm thick Teflon plate is placed at the interface between the press and a layer of elastomer. This plate helps reduce direct friction. Teflon was selected for its low friction coefficient, which effectively minimizes friction between the specimen and the press. (*iii*) A double lubricated polyethylene film layer is added to limit lateral confinement due to the elastomer.

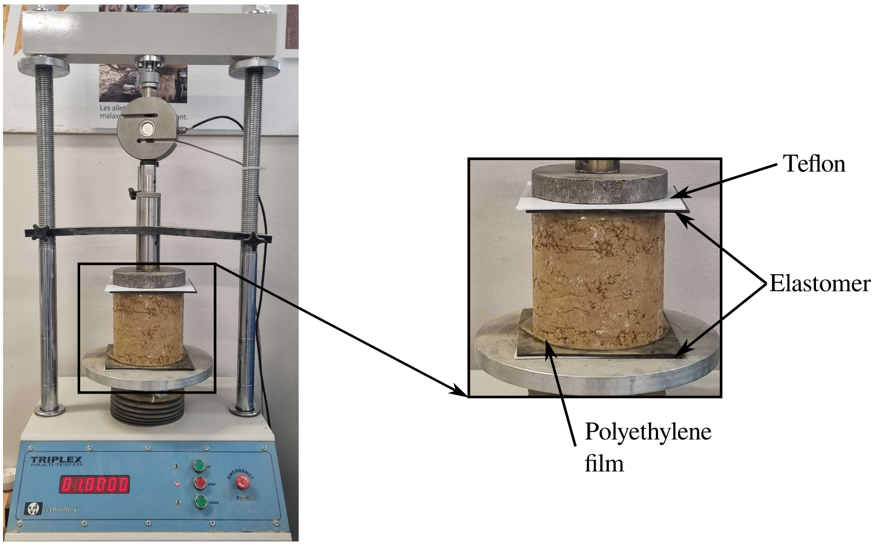

Figure 9: Specimen installation inside the uniaxial machine.

Moreover, the test was conducted under displacement control at a rate of 1 mm/min. The test was terminated after a 10% drop from the peak force to ensure that post-peak failure was captured while avoiding excessive specimen damage. It is worth mentioning that after experiments, a 1 kg sample is collected and placed in an oven at 105°C for at least 24 hours to ensure that the specimen were completely dry ($w = 0\%$).

5 Results

This section presents the experimental and numerical results obtained in this study. We first report the calculated fractal dimensions of the natural soils, followed by the compression test results for both the natural soil specimens and the AP-derived specimens. The Young's modulus of the specimens is then evaluated, showing comparable values for the AP mixtures. Finally, the numerical investigation results are presented.

5.1 Experimental results

5.1.1 Comparison of fractal dimensions of natural soils and AP

The Apollonian specimens, which was designed to follow a specified fractal particle size distribution, is compared in Figure 10 with three natural soils: CLM, STA, and SPC. These soils exhibit geometric fractal dimensions D_f greater than 2.5. Specifically, CLM has $D_f = 2.81$, STA has $D_f = 2.95$, and SPC has $D_f = 2.75$.

It is important to note that the value of D_f is highly sensitive to the particle size distribution. It is worth mentioning that higher values of D_f indicate finer and more well-graded soils, while lower values suggest coarser, more gap-graded structures (See Figure 1).

To estimate the value of D_f based on the experimental data, we analyze the particle size distribution by plotting the cumulative number of particles $N(d > d_0)$ versus particle diameter d on a log-log scale, as shown in Figure 10. If the distribution follows a power law, this plot appears as a straight line with slope D_f. For example, the pink line in the Figure 10 corresponds to the AP model with $D_f = 2.5$. The experimental data for natural soils are fitted with a coefficient of determination R^2 between 0.97 and 0.99.

Curve fitting was performed to estimate the fractal dimension D_f as the slope of the fitted line through the experimental measured points. The fitting was carried out using the Python library `SciPy` [43], specifically the `curve_fit` function, which solves a non-linear least squares problem.

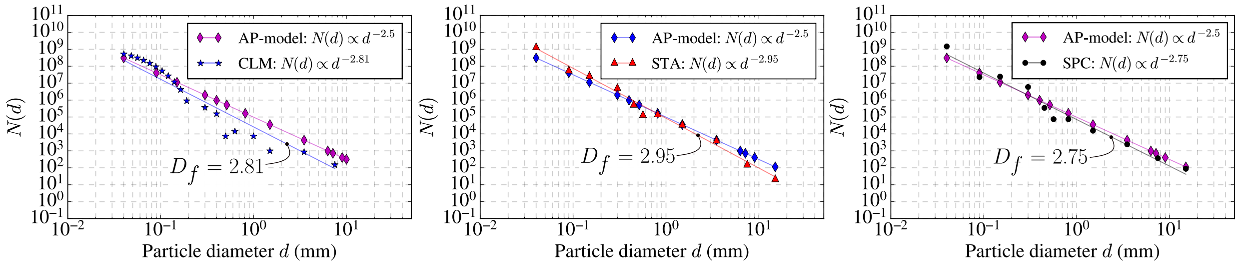

(a) (b) (c)

Figure 10: Geometric fractal dimension D_f for (a) CLM, (b) STA, and (c) SPC soils.

5.1.2 Results of compression tests

This section presents the results of uniaxial compression tests conducted on compacted soil specimens (Figure 8), divided into two groups: (1) AP specimens, designed using Apollonian particle packing with $D_f = 2.5$, and (2) natural soil specimens, characterized by a higher fractal dimension in the range between 2.75 and 2.95.

Figure 11 displays the compressive strength values obtained across three soil types under both conditions. The results reveal three key trends: (1) AP specimens are more repeatable and smoother compared to natural soil specimens, (2) AP specimens have the same compressive strength even for different soil types, and (3) specimens with higher fractal dimension exhibit higher compressive strength.

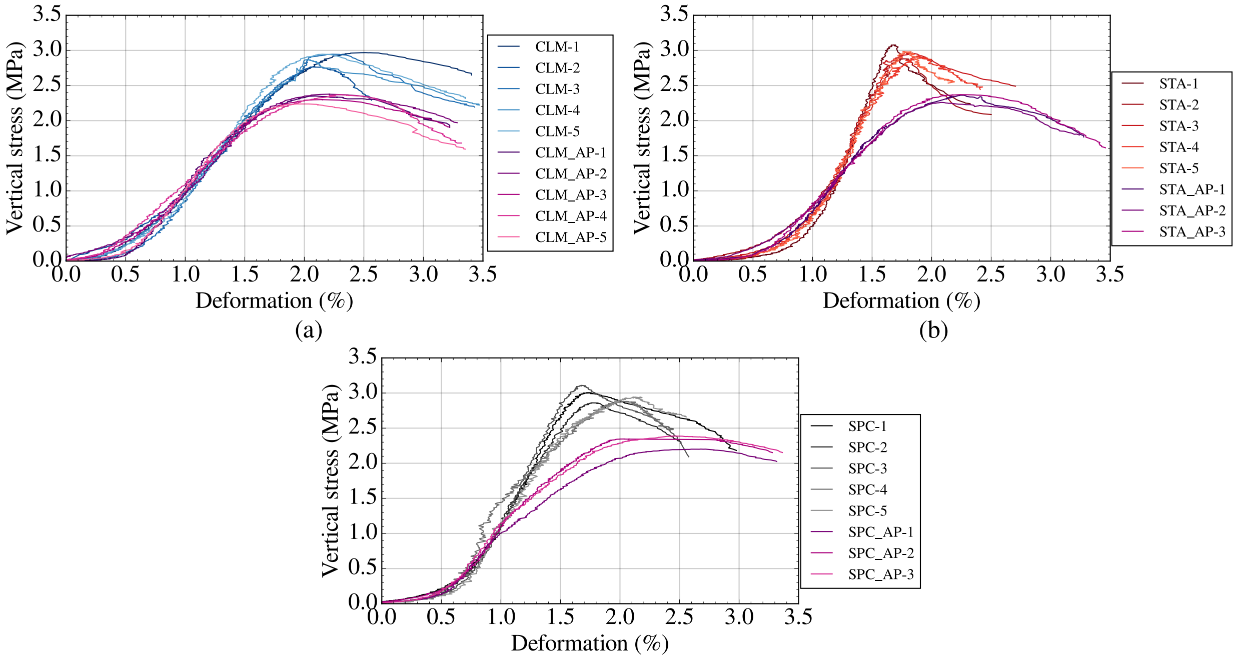

(a) (b) (c)

Figure 11: Compressive strength results for (a) CLM, (b) STA and (c) SPC specimens.

The average compressive strength of natural soil specimens was approximately 2.89 MPa for D_f between 2.75 and 2.95, compared with 2.36 MPa for AP specimens for $D_f = 2.5$ (approximately an 18% difference). Natural soils exhibited slightly higher D_f values than the reconstructed AP mixtures. Higher geometric fractal dimensions generally reflect broader particle-size distributions, which may enhance particle interlocking and load transfer and thus lead to higher compressive strength. It is worth mentioning that clay type and associated physico-chemical interactions are also known to influence soil strength [11, 34]. Since detailed mineralogical analyses (e.g., X-ray diffraction) were not performed in the present work, the influence of clay type on the compressive strength cannot be isolated.

According to Table 6, AP specimens exhibited lower variability in compressive strength than natural soils, as reflected by the smaller standard deviation within each soil type. Although some variation was observed between AP groups (0.029 MPa), it remained significantly lower than that measured for the natural soil specimens (0.087 MPa). This reduction in scatter suggests that the controlled particle-size distribution imposed by the Apollonian packing approach promotes more consistent packing conditions between specimens. In addition, natural soils were measured to have slightly higher variability, possibly due to the difference in particles distribution between specimens.

Moreover, AP specimens prepared from different soils can exhibit similar compressive strengths when they share the same fractal dimension. The AP reconstruction imposes a common structural organization that tends to reduce the influence of the physical properties among different soils.

Table 6: Summary of mean and standard deviation of vertical stress and density for specimens with and without AP.

specimens type	AP	Vertical stress (MPa)	Density (g/cm^3)
CLM	No	2.899 ± 0.084	2.000 ± 0.016
	Yes	2.327 ± 0.058	2.006 ± 0.005
STA	No	3.0 ± 0.100	2.012 ± 0.002
	Yes	2.341 ± 0.071	1.983 ± 0.003
SPC	No	2.930 ± 0.265	2.180 ± 0.000
	Yes	2.385 ± 0.106	2.167 ± 0.006

To further assess the impact of geometric fractal dimension (D_f) on soil mechanical performance, a second series of experimental tests was conducted using STA soil. Two mixtures were prepared whose specifications had particle size distributions of $D_f = 2.25$ and $D_f = 2.75$. STA soil was selected for this analysis because its particle size distribution (See Figure 4) is between the finer CLM and coarser SPC soils, and thus, it can be considered as an intermediate condition. The mixtures underwent modified Proctor tests to obtain compaction properties. For both mixtures, the maximum dry densities were 2.03 g/cm^3 at 10% water content for $D_f = 2.25$, and 2.04 g/cm^3 at 10.5% for $D_f = 2.75$.

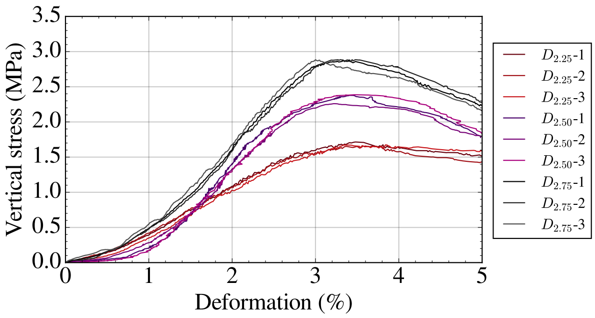

Figure 12: Vertical stress results for STA specimens with different D_f values.

The vertical stress results are summarized as follows (see Figure 12):

- $D_f = 2.25$: 1.68–1.72 MPa (mean: 1.70 MPa)
- $D_f = 2.50$: 2.26–2.39 MPa (mean: 2.34 MPa)
- $D_f = 2.75$: 2.88–2.91 MPa (mean: 2.89 MPa)

These results, illustrated in Figure 12, demonstrate two key trends. First, the Apollonian-based specimens are highly repeatable, with very low scatter within each D_f group, confirming the reproducibility of the packing concept and confirming the previous results obtained for AP specimens. Second, compressive strength increases systematically with fractal dimension, indicating that higher D_f values enhance the stress-transfer capacity by creating denser particle frameworks. Overall, increasing D_f from 2.25 to 2.75 yields a 1.19 MPa (70%) increase in compressive strength.

Despite the differences in compressive strength, all specimens exhibited similar mechanical behavior, with comparable failure modes (see Figure 13). The observed failures were characterized by typical shear-dominated cracking patterns commonly reported in compacted granular materials. This suggests that variations in the fractal dimension D_f primarily influence the magnitude of the compressive strength through changes in particle packing and interparticle contact density, while the overall macroscopic failure mechanism remains governed by the same shear-dominated deformation process.

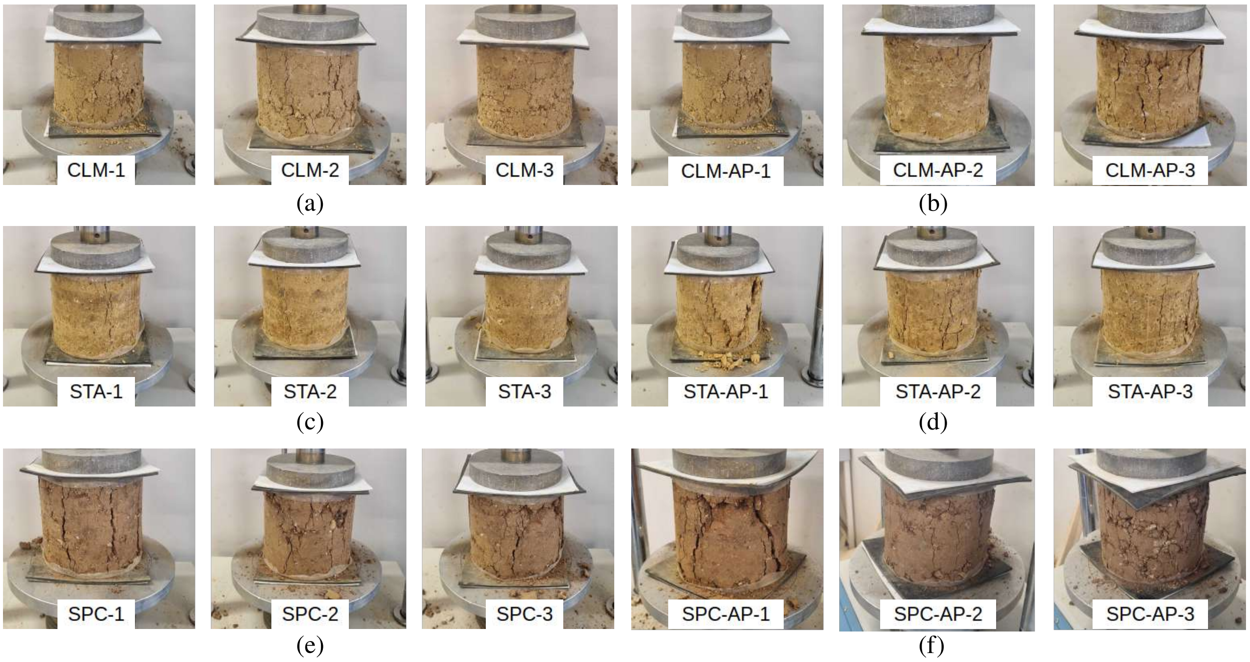

Figure 13: specimens failure, (a) CLM, (b) CLM-AP, (c) STA, (d) STA-AP, (e) SPC, and (f) SPC-AP.

In Figure 14, the experiments demonstrate that dry density correlates well with mechanical strength, for the same soil. For all tested dry soil types, specimens of equivalent dry density exhibited large variances in compressive strength which demonstrates that microstructural aspects beyond bulk density, including particle organization, clay activity, and effective load-bearing skeleton, has main influences [3, 9, 27, 35]. This characteristic is even more pronounced in the AP mixtures: despite differences in dry density across soils and AP target dimensions, compressive strength results commonly resulted in similar values which indicates geometrically optimized packing, and clay content governs strength far more than overall density. For the same soil, by changing the fractal dimension D_f, the resultant compressive strength could be drastically different despite having the same packing density values which would further support the interpretation that ultimately the internal packing architecture, coordination number, and distribution of fines materially affects strength more than total mass per unit volume.

From an engineering point of view, these results suggest that the mechanical performance of rammed earth could potentially be enhanced through a controlled particle size distribution during soil preparation. In practice this can be done by using a ratio of coarse, sand and fine fractions when selecting or mixing soil in order to achieve gradations closer to those with higher fractal dimensions. Gradation control of this type is already employed in earth construction by adding or removing either the sand or gravel fractions from the mix, and this work establishes a quantitative basis for relating these gradations to probable strength improvements.

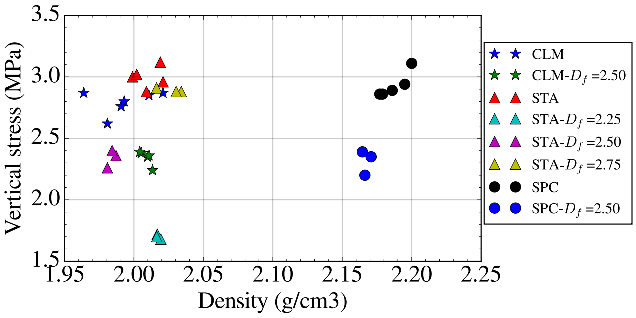

Figure 14: Compressive strength results as function of density for CLM, STA and SPC specimens.

5.1.3 Young's modulus of rammed earth specimens

Rammed earth presents a reasonably broad range of elastic stiffness (Young's modulus), highly dependent upon moisture, compaction energy, soil composition (clay content, sand/gravel and fines), dry density. For example, Dialmy et al. [14] report values of E for rammed earth range from approximately 60 MPa up to 1000 MPa, they also reported values within 150–500 MPa under standard or typical conditions (meaning optimum compaction and moderate moisture conditions). Sabba et al. [40], report Young's modulus values between 65 and 78 MPa (for unstabilized or lightly modified mixes) values with compressive strengths around 2.6 MPa. Additionally, Bui et al. [10] provide Young's modulus for (on-site) rammed earth walls around 100 MPa for old walls, while new/recent walls of similar components values are close to 500 MPa.

In our experiments, as shown in Figure 11, our stress-strain (strain equal to deformation/100) curves have two slopes. The first (lower) slope (between 0 and 1% deformation), stands for the phase during which the sample comes into contact with the press, with the applied force being resumed. The second (steeper) slope occurs during the linear elastic phase for the specimen under load. Therefore, in our experiments we consider the slope of the second part and Young's modulus E was calculated and summarized in Table 7. For STA with D_f equal to 2.25 the E equal to 109.36 ± 4.1 MPa, and for D_f equal to 2.75 the E equal to 187.0 ± 3.9 MPa.

Table 7: Young's modulus (MPa) (mean ± SD) for CLM, STA and SPC, with and without AP.

Soil type	E (MPa)	
	without AP	with AP
CLM	212 ± 15	201 ± 12
STA	296 ± 24	216 ± 8
SPC	275 ± 34	197 ± 15

The Young's modulus results show that AP specimens exhibit relatively consistent stiffness values, with an average of about 205 MPa. In comparison, AP specimens generally present lower stiffness than the corresponding natural soils, with reductions of approximately 5% (CLM), 37% (STA), and 39% (SPC).

Within the STA–AP mixtures, an increase in the fractal dimension (D_f) from 2.25 to 2.75 is associated with an increase in stiffness from 110 ± 5 MPa to 187 ± 4 MPa. Overall, the results suggest that the AP approach leads to more consistent mechanical responses, while the influence of D_f on stiffness appears to be dependent on the specific soil and mixture conditions. These observations indicate that particle packing geometry influence the elastic behavior of the material, although it cannot be considered as the sole controlling factor (others like clay type, physcial properties).

5.2 Numerical investigation

5.2.1 Data generation

The input from the materials characterization and experimental results yields at most five results per test, necessitating additional data generation for the MLP model. In this context, fitting complex probability distributions is unreliable for such limited datasets. A more robust approach is to adopt a non-parametric, descriptive method, to represent the datasets in the simplest distribution possible by considering the range of the observations, i.e., uniform distribution. This conservative strategy is used to generate new data points between the observed minimum and maximum, avoiding potentially misleading assumptions about central tendency or skewness. The characterization of the materials is summarized in Figure 15, which illustrates the mean, variability, and overall range of each material's properties, corresponding to specimens fabricated from natural materials as well as materials treated using the applied AP method, denoted as the natural material name -AP(D_f value).

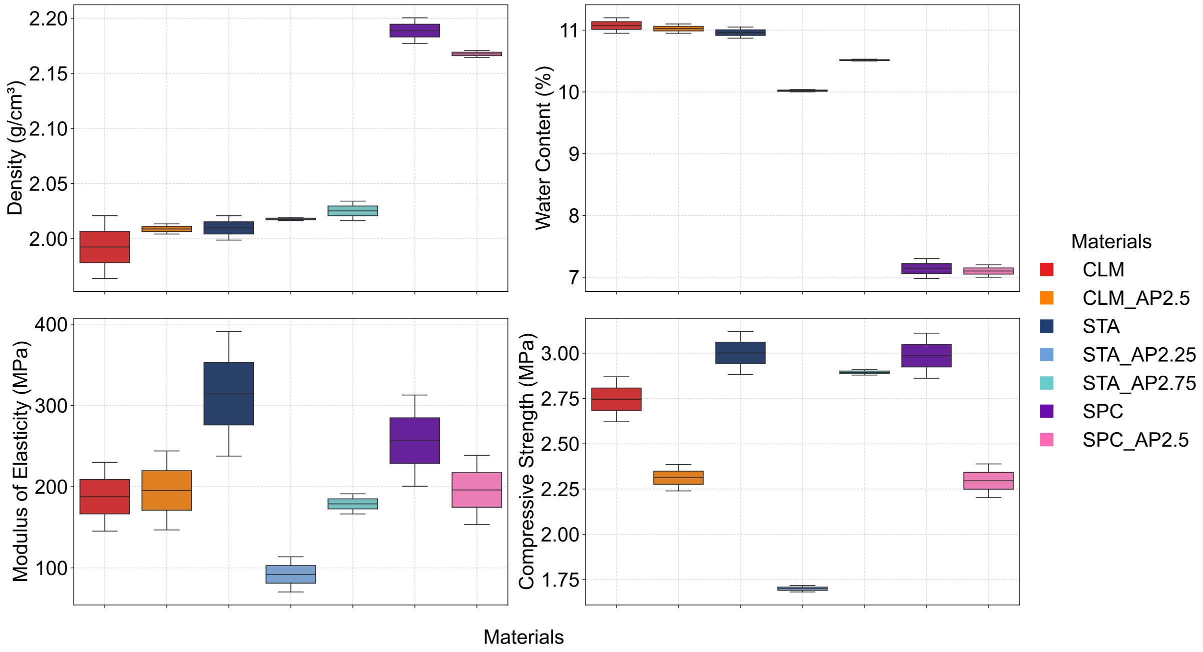

Figure 15: Materials properties.

5.2.2 Statistical relevance of input features

The best-fitting MLP model, defined in the Methodology Section 2.2, was trained through a loop of systematic hyperparameter grid search, evaluating multiple configurations of input features (D_f, density, water content, and modulus of elasticity), activation functions, solvers, L2 regularization coefficients, several architectures, i.e., the number of hidden layers and neurons per layer. This is followed by performing the SHAP (SHapley Additive exPlanations) analysis to offer a scientifically rigorous measure of features importance rather than simple univariate correlation, as shown in Figure 16. This analysis reveals the relative importance of the input features and quantifies the nonlinear contribution of the input features to the target, i.e., compressive strength learned by the network. The results of the SHAP ranking indicate that D_f is the most influential variable, followed by the density, water content, and modulus of elasticity within the optimal model performance.

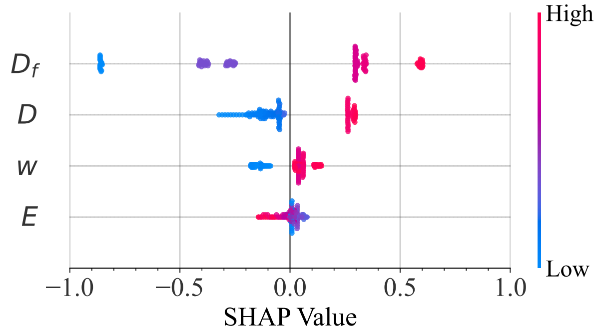

Figure 16: Input features importance.

5.2.3 Model performance

The MLP model demonstrated excellent predictive performance across the training and testing phases, as illustrated by the density distribution and parity plots, shown in Figure 17. The results of the density distribution for both the training and the testing sets (Figure 17a) show that the intensity of the predicted compressive strength closely follows the distribution of the actual values, capturing the shape and peak intensities for each interval of actual value. The results indicate that the model successfully learned the underlying pattern without overfitting and also confirms the ability of the model to generalize unknown data. The values predicted from the MLP model are presented alongside the actual values in Figure 17b to visualize the variations and assess the fitting. The results support the previous conclusion, where the points are aligned along the linear 1:1 line, demonstrating high accuracy and low bias in the predictions.

Quantitative performance indicators (Table 8) confirm the high precision and generalizability of the model. The results indicate small deviations between the predicted and actual compressive strength across all the data, in which the model explains nearly all the variance in the experimental data, demonstrated by a high R^2 value.

Table 8: Model performance metrics

Dataset	**MAE**	**RMSE**	**R^2**
Train	0.0034	0.0043	0.9999
Test	0.0040	0.0057	0.9999

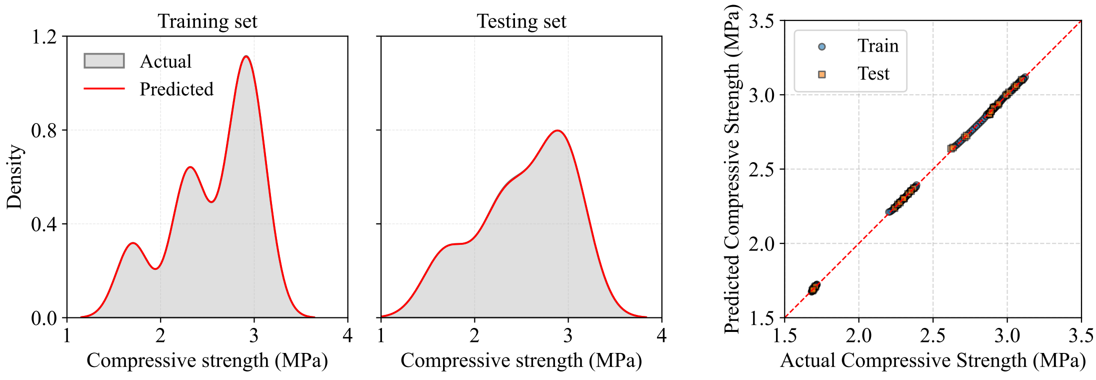

(a) **(b)**

Figure 17: Model performance: (a) density distribution of training and testing sets, and (b) actual vs predicted compressive strength.

5.2.4 Prediction for the studied materials

The predictive robustness of the model is evaluated by comparing the predictions of the compressive strength to their actual values across the full dataset. Figure 18 presents the density distributions of the predicted compressive strength and their corresponding actual distributions for all materials. For the CLM and SPC specimens, the predicted distributions closely overlap with the actual distributions, where the predicted mean aligns well with the actual central tendencies. For the STA_AP formulations, the distributions indicate a consistent agreement on the mean aligning well with the actual central tendency, while the spread of the predictions is slightly less (0.025-0.015 MPa) than the actual spread, causing an increase in the intensity around the mean. The results indicate the robustness of the model in handling material variations when predicting the compressive strength.

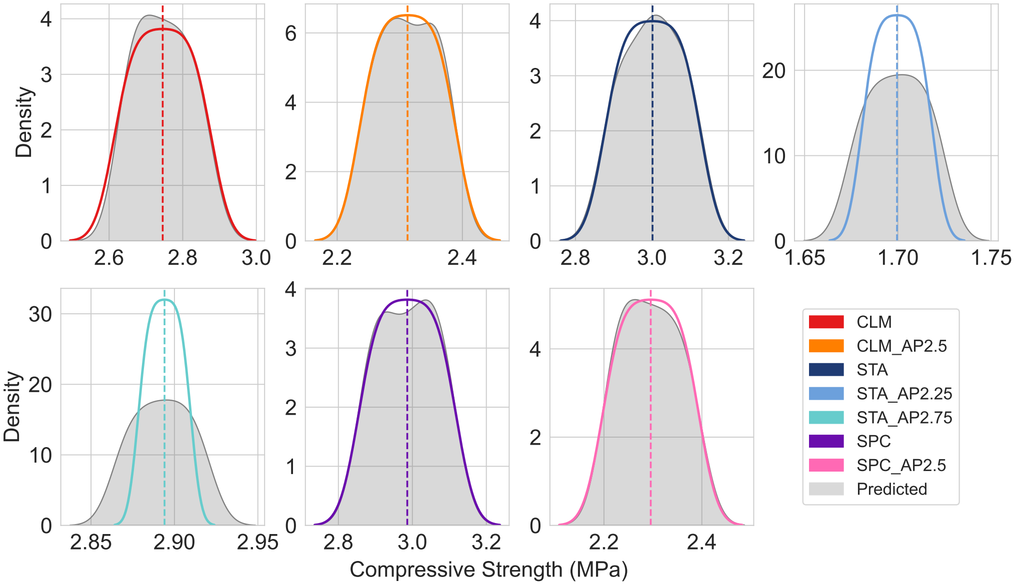

Figure 18: Density distributions of actual and predicted compressive strength per material.

Figure 19 presents a visualization of the residuals distribution of the model predictions for all the materials. The residuals are centered around zero, indicating miminal systematic bias in the predictions, where the majority of residuals falls within the range of ±0.005 MPa, demonstrating a very small prediction error. The quantitative performance indicators per material in Table 9 indicate small deviations between the predicted and actual compressive strength per material across all the dataset, confirming the robustness of the model in handling material variations when predicting the compressive strength.

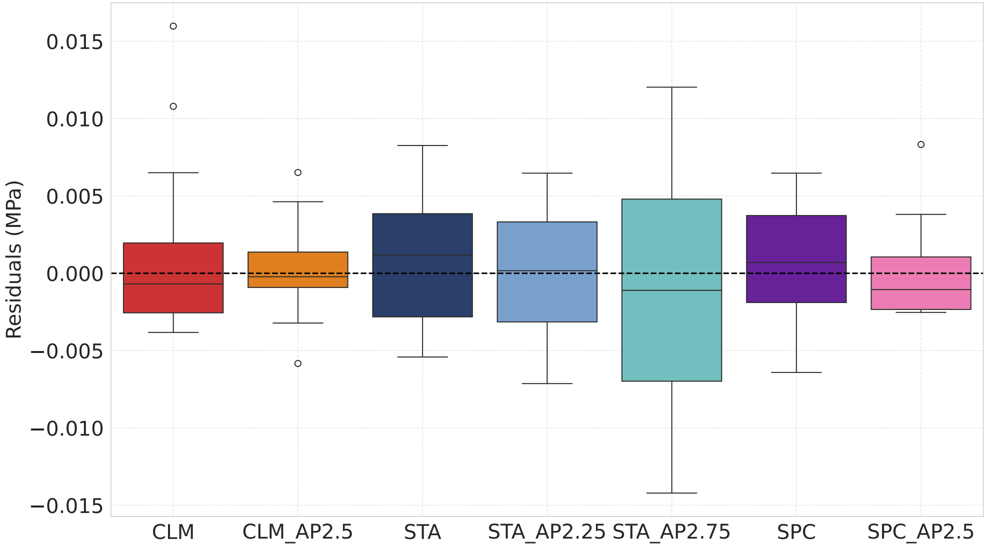

Figure 19: Residuals of model predictions per material.

Table 9: Prediction error indicators by material

Material	MAE	RMSE
CLM	0.003392	0.005043
CLM_AP 2.5	0.001900	0.002674
STA	0.003690	0.004229
STA_AP 2.25	0.003457	0.004023
STA_AP 2.75	0.006448	0.007586
SPC	0.003293	0.003872
SPC_AP 2.5	0.002124	0.002685

5.2.5 Application for a new material

This section studies the MLP model capability in predicting the compressive strength of a new material formulation that was not considered during the training of the model, i.e., STA_AP2.5. Figure 20 illustrates the density distribution of the predicted and actual STA_AP2.5 material formulation. The results indicate a strong alignment with the distribution, with only a slight shift in central tendency of approximately 0.01 MPa, which in turn results in a minor change in the spread of the distribution of about 0.005 MPa. The quantitative error indicators of the prediction of the new formulation material are presented in Table 10. The results indicate small deviations between the predicted and actual compressive strength of the newly presented material formulation, where the model explains well the variance in the experimental data, demonstrated by the high R^2 value. Therefore, the results indicate that the model remains highly reliable when applied to new material formulations.

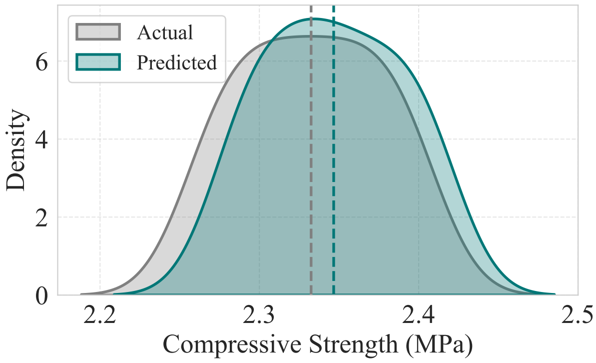

Figure 20: Density distribution of prediction and actual values of the STA-AP ($D_f = 2.5$) material formulation.

Table 10: Performance metrics of the validation.

Metric	**Value**
MAE	0.014169
RMSE	0.014312
R²	0.891197

6 Conclusions

This study evaluated the influence of the Apollonian Packing (AP) concept on the compressive behavior of rammed earth materials. A total of 32 cylindrical specimens were prepared experimentally, including 17 specimens incorporating AP-designed particle-size distributions and 15 specimens composed of naturally graded soils. All specimens were compacted at the modified Proctor optimum water content and subsequently tested in a dry condition.

The results show that natural soils with higher fractal dimensions (D_f between 2.75 and 2.95) exhibited compressive strengths approximately 18% higher than the AP mixtures with $D_f = 2.5$. However, the AP-designed specimens displayed reduced variability and improved repeatability in compressive strength results. This behavior is associated with the controlled particle-size distribution imposed by the AP gradation, which promotes more consistent packing conditions between specimens.

Although the three natural soils (CLM, STA, and SPC) present different physical and physicochemical characteristics, their AP-reconstructed mixtures exhibited comparable compressive strengths when prepared with similar fractal dimensions. This observation suggests that, under dry conditions and within the range of materials investigated, particle packing geometry characterized by D_f plays an important role in the mechanical response, although mineralogical and physicochemical effects may also influence behavior and were not fully isolated in this study.

The machine learning analysis based on a multilayer perceptron (MLP) model successfully captured the nonlinear relationships between soil descriptors and compressive strength. The model demonstrated strong predictive capability, including accurate estimation of the compressive strength of an additional formulation (STA-AP with $D_f = 2.5$), with a mean absolute error of 0.014 MPa.

From an engineering perspective, the results indicate that controlling particle-size distribution to approach higher effective fractal dimensions may provide a practical strategy for improving the mechanical performance of rammed earth materials through optimized gradation design. Future work should further investigate the role of mineralogical composition and moisture conditions, including tests under partially saturated states, in order to better represent field conditions and to refine the applicability of fractal-based particle organization in sustainable earth construction.

References

[1] H. Abdelmonem, M. Bakr, and M. Eldin. Influence of water content on the shear strength parameters for cohesive soil. *Journal of Al-Azhar University Engineering Sector*, 18:529–540, 07 2023. doi: 10.21608/auej.2023.310316.

[2] AFNOR. Sols : reconnaissance et essais – essai proctor normal et modifié. Technical Report NF P 94-093, Association française de normalisation (AFNOR), Paris, France, 1999.

[3] E. Anglade. *Évaluation des performances des matériaux en terre crue par homogénéisation poro-mécanique analytique non linéaire.* PhD thesis, Université Paul Sabatier (Toulouse III), 2022. URL https://tel.archives-ouvertes.fr/tel-03772196v1.

[4] S. V. Anishchik and N. N. Medvedev. Three-dimensional apollonian packing as a model for dense granular systems. *Physical Review Letters*, 75:4314–4317, 1995. doi: 10.1103/PhysRevLett.75.4314.

[5] ASTM D2487. Standard practice for classification of soils for engineering purposes (unified soil classification system). Technical Report ASTM D2487, ASTM International, West Conshohocken, PA, USA, 2017.

[6] J.-E. Aubert, P. Faria, P. Maillard, K. Ouedraogo, C. Ouellet-Plamondon, and E. Prud'homme. *Characterization of Earth Used in Earth Construction Materials*, pages 17–81. , 01 2022. ISBN 978-3-030-83296-4. doi: 10.1007/978-3-030-83297-1_2.

[7] F. Ávila, E. Puertas, and R. Gallego. Characterization of the mechanical and physical properties of unstabilized rammed earth: A review. *Construction and Building Materials*, 270:121435, 2021. doi: 10.1016/j.conbuildmat.2020.121435.

[8] R. Bahar, M. Benazzoug, and S. Kenai. Performance of compacted cement-stabilised soil. *Cement and Concrete Composites*, 26(7):811–820, 2004. ISSN 0958-9465. doi: https://doi.org/10.1016/j.cemconcomp.2004.01.003. URL https://www.sciencedirect.com/science/article/pii/S0958946504000058.

[9] H. Bamogo, M. Ouedraogo, I. Sanou, K. A. J. Ouedraogo, K. Dao, J.-E. Aubert, and Y. Millogo. Improvement of water resistance and thermal comfort of earth renders by cow dung: an ancestral practice of burkina faso. *Journal of Cultural Heritage*, 46:42–51, 2020. ISSN 1296-2074. doi: https://doi.org/10.1016/j.culher.2020.04.009. URL https://www.sciencedirect.com/science/article/pii/S1296207420300509.

[10] Q. B. Bui, S. Hans, J.-C. Morel, and P. do. First exploratory study on dynamic characteristics of rammed earth buildings. *Engineering Structures*, 33:3690–3695, 12 2011. doi: 10.1016/j.engstruct.2011.08.004.

[11] J. Canivell, J. Martín-del Río, R. Falcón, and C. Rubio-Bellido. Rammed earth construction: A proposal for a statistical quality control in the execution process. *Sustainability*, 12:1–22, 04 2020. doi: 10.3390/su12072830.

[12] P.-A. Chabriac. *Mesure du comportement hygrothermique du pisé*. PhD thesis, École Nationale des Travaux Publics de l'État (ENTPE), 2014. URL `https://hal.science/tel-01413611`.

[13] J. de Bono and G. McDowell. On the micro mechanics of one-dimensional normal compression. *Géotechnique*, 63:895, April 2013. doi: 10.1680/geot.12.P.041.

[14] A. Dialmy, M. Rguig, and M. Meliani. Optimization of the granular mixture of natural rammed earth using compressible packing model. *Sustainability*, 15(3), 2023. ISSN 2071-1050. doi: 10.3390/su15032698. URL `https://www.mdpi.com/2071-1050/15/3/2698`.

[15] Earth Architecture. The great mosque of djenne. `https://eartharchitecture.org/?p=1071`, 2024. Accessed: 2025-01-10.

[16] Encyclopaedia Britannica. Apollonius of perga. `https://www.britannica.com/biography/Apollonius-of-Perga`, February 2024.

[17] Encyclopædia Britannica. Alhambra. `https://www.britannica.com/topic/Alhambra-fortress-Granada-Spain`, 2024. Accessed: 2025.

[18] Encyclopædia Britannica. Great wall of china. `https://www.britannica.com/topic/Great-Wall-of-China`, 2025. Accessed: 2025.

[19] R. Filgueira, L. Fournier, C. Cerisola, P. Gelati, and M. García. Particle-size distribution in soils: A critical study of the fractal model validation. *Geoderma*, 134:327–334, 10 2006. doi: 10.1016/j.geoderma.2006.03.008.

[20] Focus Work. L'orangerie – lyon confluence. `https://www.focus.work/nos-espaces/lorangerie-lyon-2-confluence/`, 2025. Accessed: 2025-02-15.

[21] Global Cement and Concrete Association (GCCA). Cement industry net zero progress report 2024/25. Report, Global Cement and Concrete Association, April 2024. URL `https://gccassociation.org/cement-industry-net-zero-progress-report-2024-25`.

[22] H. Guillaud and H. Houben. *Traité de construction en terre*. Parenthèses, 1989.

[23] B. Habeeb, E. Bastidas-Arteaga, M. Sánchez-Silva, and Y. Dong. Conditional seasonal markov-switching autoregressive model to simulate extreme events: Application to river flow. *Environmental Modelling & Software*, 178:106066, 2024. doi: 10.1016/j.envsoft.2024.106066.

[24] C. Hecht. Appolonian packing and fractal shape of grains improving geomechanical properties in engineering geology. *Pure and Applied Geophysics*, 157:487–504, 04 2000. doi: 10.1007/PL00001103.

[25] E. A. Holm, R. Cohn, N. Gao, A. R. Kitahara, T. P. Matson, B. Lei, and S. R. Yarasi. Overview: Computer vision and machine learning for microstructural characterization and analysis. *Metallurgical and Materials Transactions A*, 51(12):5985–5999, 2020.

[26] C. H. Kouakou and J.-C. Morel. Strength and elasto-plastic properties of non-industrial building materials manufactured with clay as a natural binder. *Applied Clay Science*, 44(1):27–34, 2009. doi: 10.1016/j.clay.2008.12.019.

[27] A. Laborel-Préneron, J.-E. Aubert, C. Magniont, C. Tribout, and A. Bertron. Plant aggregates and fibers in earth construction materials: A review. *Construction and Building Materials*, 111:719–734, 2016. doi: 10.1016/j.conbuildmat.2016.02.119.

[28] D. C. Liu and J. Nocedal. On the limited memory bfgs method for large scale optimization. *Mathematical Programming*, 45(1):503–528, 1989. doi: 10.1007/BF01589116.

[29] Malvernp Panalytical. Mastersizer range. www.malvernpanalytical.com, 2025.

[30] S. S. Manna and H. J. Herrmann. Precise determination of the fractal dimensions of apollonian packing and space-filling bearings. *Journal of Physics A: Mathematical and General*, 24(9):L481, 1991. doi: 10.1088/0305-4470/24/9/006.

[31] J.-C. Morel, A. Pkla, and P. Walker. Compressive strength testing of compressed earth blocks. *Construction and Building Materials*, 21(2):303–309, 2007. doi: 10.1016/j.conbuildmat.2005.08.021.

[32] Y. M. H. Mustafa, M. S. Zami, O. S. B. Al-Amoudi, M. A. Al-Osta, and Y. S. Wudil. Analysis of unconfined compressive strength of rammed earth mixes based on artificial neural network and statistical analysis. *Materials*, 15(24):9029, 2022. doi: 10.3390/ma15249029.

[33] A. P. Nowak, M. Pierzchalski, and J. Klimowicz. Circular economy in rammed earth construction: A life-cycle case study on demolition and reuse strategies of an experimental building in pasłęk, poland. *Sustainability*, 18(2), 2026. doi: 10.3390/su18020790.

[34] M. Olivier. *Le matériau terre, compactage, comportement, application aux structures en bloc sur terre*. PhD thesis, INSA Lyon, 1994. URL http://www.theses.fr/1994ISAL0004.

[35] J. A. K. Ouedraogo, J.-E. Aubert, C. Tribout, and G. Escadeillas. Is stabilization of earth bricks using low cement or lime contents relevant? *Construction and Building Materials*, 236:117578, 03 2020. doi: 10.1016/j.conbuildmat.2019.117578.

[36] A. Pelé-Peltier, A. Fabbri, J.-C. Morel, E. Hamard, and M. Lhenry. A similitude relation to assessing the compressive strength of rammed earth from scale-down samples. *Case Studies in Construction Materials*, 16:e00921, 2022. doi: 10.1016/j.cscm.2022.e00921.

[37] A. Pinkus. Approximation theory of the mlp model in neural networks. *Acta numerica*, 8:143–195, 1999.

[38] M. H. Rafiei, W. H. Khushefati, R. Demirboga, and H. Adeli. Neural network, machine learning, and evolutionary approaches for concrete material characterization. *ACI Materials Journal*, 113(6), 2016. doi: 10.14359/51689213.

[39] S. Ravindran and I. Gratchev. Effect of water content on apparent cohesion of soils from landslide sites. *Geotechnics*, 2(2):385–394, 2022. doi: 10.3390/geotechnics2020021.

[40] M. F. Sabbà, M. Tesoro, C. Falcicchio, and D. Foti. Rammed earth with straw fibers and earth mortar: Mix design and mechanical characteristics determination. *Fibers*, 9(5):30, 2021. doi: 10.3390/fib9050030.

[41] A. Stoll and P. Benner. Machine learning for material characterization with an application for predicting mechanical properties. *GAMM-Mitteilungen*, 44(1):e202100003, 2021. doi: 10.1002/gamm.202100003.

[42] C. Swalec and E. Torres Morales. A matter of transparency: 2024 insights on the steel industry's evolving commitments to reach net zero by 2050. Briefing, Global Energy Monitor and LeadIT, October 2024. URL https://www.industrytransition.org/insights/slow-progress-on-net-zero-targets-amongst-the-largest-steel-producers/.

[43] P. Virtanen, R. Gommers, T. E. Oliphant, M. Haberland, T. Reddy, D. Cournapeau, E. Burovski, P. Peterson, W. Weckesser, J. Bright, et al. Scipy 1.0: fundamental algorithms for scientific computing in python. *Nature Methods*, 17(3):261–272, 2020.

[44] J. Yu, X. Lv, B. Ma, H. Wu, S. Du, M. Zhou, Y. Yang, and G. Han. Fractal features of soil particle size distribution in newly formed wetlands in the yellow river delta. *Scientific Reports*, 5, 2015. doi: 10.1038/srep10540.

[45] Z. Zhang, X. Fu, W. Yuan, Q. Sheng, S. Chai, and Y. Du. The influence of the fractal dimension on the mechanical behaviors of the soil–rock mixture: A case study from southwest china. *Fractal and Fractional*, 7(2), 2023. doi: 10.3390/fractalfract7020106.